A 3D-Bioprinted Vascularized Glioblastoma-on-a-Chip for Studying the Impact of Simulated Microgravity as a Novel Pre-Clinical Approach in Brain Tumor Therapy

Giulia Silvani, Carin Basirun, Hanjie Wu, Christine Mehner, Kate Poole, Peta Bradbury, and Joshua Chou*

Glioblastoma multiforme (GBM) is one of the most aggressive malignant brain tumors and urgently requires the development of new therapeutic strategies. In this study, an innovative hybrid in vitro vascularized GBM-on-a-chip model is presented as a strategic integration of microfluidics and 3D bioprinting technologies. The system can recreate the compartmentalized brain tumor microenvironment, comprising the functional blood brain barrier (BBB) and the adjacent 3D perivascular tumor niche, by selectively mimicking physiological shear stress and cell–cell, cell–matrix mechanical interaction. The GBM-on-a-chip model was evaluated under simulated microgravity (μG) condition as a form of mechanical unloading showing a significant cell morphological and mechanotransduction response thereby indicating that gravitational forces play an important role in glioblastoma mechanical regulation. The proposed GBM-on-a-chip represents a meaningful biological tool for further research in cancer mechanobiology and pre-clinical approach in brain tumor therapy.

1. Introduction

Glioblastoma multiforme (GBM) is a fast-growing, aggressive glioma (grade IV) that originates in the central nervous system from astrocytes.[1] GBM accounts for ≈17% of all brain tumors in adults with a median overall survival rate of 16–21 months following diagnosis.[2,3] Several factors are known to limit the success of current GBM therapies, including inaccessible tumor localization within the brain, high rate of malignant cells invasion into adjacent brain tissue, and inherent resistance to conventional therapy.[4–6] Compared to other aggressive tumors, which metastasize through the circulatory system thus affecting different organs within the body, high-grade GBM rarely metastasize, rather actively migrate, and proliferate into spherical shape (spheroids) within healthy brain tissue and perivascular space.[7] However, the growing tumor masses within the brain, often far from brain vasculatures, lead to an ineffective dosage of chemotherapeutics that can access the malignant cells.[8] The brain vasculature forms a highly specialized structure commonly referred as the blood brain barrier (BBB) with the fundamental role in protecting and maintaining the homeostasis of the brain.[9,10] Non-fenestrated brain endothelial cells line the innermost surface of these blood vessels and are tightly connected by protein-complexes, forming a continuous selective biological barrier thus preventing leakage of transported solutes.[11–13] At the cell–cell border, these structures known also as inter-endothelial tight junctions or zonulae occludens (ZO)[14,15] dynamically integrate with associated signaling molecule[16] and the actin cytoskeleton, enabling rapid remodeling in response to external mechanical stimuli, such as the shear stress arising from blood flow.[17–20] Working as both a physical and a biochemical barrier to protect the brain from

G. Silvani, C. Basirun, H. Wu, J. Chou
School of Biomedical Engineering, Faculty of Engineering and Information Technology
University of Technology Sydney
Sydney, Australia
E-mail: Joshua.chou@uts.edu.au

C. Mehner
Department of Physiology and Biomedical Engineering
Mayo Clinic
Jacksonville, FL, USA

K. Poole
EMBL Australia node in Single Molecule Science, School of Medical Sciences, Faculty of Medicine
University of New South Wales
Sydney 2052, Australia

P. Bradbury
Institut Curie, Paris Sciences et Lettres Research University
Mechanics and Genetics of Embryonic and Tumoral Development Group
Paris, France

**ADVANCED
SCIENCE NEWS**

www.advancedsciencenews.com

**ADVANCED
THERAPEUTICS**

www.advtherap.com

harmful elements present in the blood, this effective barrier also significantly inhibits the diffusion of large molecules, such as chemotherapeutics, limiting their therapeutic efficacy.[21] The structural organization of brain tumors and the functional BBB constitute a major challenge in GBM treatment and at the same time lead to the urgent need in developing alternative effective chemotherapeutic strategies.[22,23]

Physical and mechanical forces exerted on cells by their microenvironment can play a significant role in regulating the balance between cellular physiology and pathology.[24,25] The mechanical loading arising from the persistent gravity vector has influenced the evolution, growth and differentiation of all Earth lifeforms. It has been shown that the mechanical unloading experienced via real or simulated microgravity can affect a wide range of biological functions ranging from cell–molecular to tissues, and to the entire organism as a whole.[26,27] Interestingly, recent research has also identified phenotypic changes in pathological models of tumors including alterations in cell adhesion properties, cell shape, and viability,[28–33] suggesting that tumorigenesis may be influenced by gravity-dependent mechanisms. Furthermore, these data indicates that gravity, as a mechanical stimulus, plays a more extensive role than previously thought, thus expanding the paradigm of cellular mechanotransduction in tumor behavior.[8,34–36] A current challenge in brain tumor therapy for enhanced drug delivery is to understand the regulation of vascular integrity and permeability in response to both intercellular (fluid shear flow) and external (gravity) mechanical forces.[37–41] The importance of cell mechanics in these processes poses the open question: can the application of a µG state, thus a mechanical unbalance of forces, disrupt the inter-endothelial junction of the BBB layer and induce a temporary enhanced permeability to chemotherapeutics?

The development of innovative and reliable chemotherapeutic strategies requires sophisticated in vitro models to emulate the pathophysiology of the complex biological microenvironment.[42] To date, several 3D cell culture systems have been proposed, including organs-on-chip and 3D bioprinting technologies.[43,44] Although both deliver on the same promise of high-fidelity 3D tissue generation, they differ in reproducibility, high-throughput readouts, and spatiotemporal control. Organs-on-chip is a well-established microfluidic-based technology which can provide features that more closely resemble mechanical or chemical in vivo conditions of vasculature-like structure.[45–48] This includes the control over the application of hydrodynamic forces, local mechanical properties, and soluble signal gradients. However, in terms of physiological complexity, organs-on-a-chip devices remain inferior to bioprinted models. Bioprinting has recently emerged as an additional promising technology for development of in vitro tumor models.[49–52] This technology relies on a high level of faithful in recapitulating the 3D organization of multiple cell population into engineered biomaterials. In this way, self-organization into physiological architecture, for example, the native tumor microenvironment, is favored. In contrast, organs-on-a-chip approaches refer to precise location of cell, often performed in artificial manner. However, organs-on-a-chip are high-throughput systems through microscopy, mechanical measurements, and other analytical systems, while 3D bioprinted constructs are still subjected to screenable readouts challenges. As a promising and revolutionary approach, the strategic inte-

gration of 3D bioprinting tissue within microfluidic bioreactor can address each of the approaches limitation and improve the flexibility of constructing tissues for experimental and clinical needs.[53] The brain tumor micro-environment, which includes vascularization and 3D complex structure of the tumor itself, dictates the necessity for an equally advanced cellular model to truly unravel the underlying function and mechanism. However, the convergence of organ-on-chip coupled with bioprinting is still in its infancy and few studies have demonstrated the improvements of such biological models in brain cancer research.[54,55]

In this study, a synergistic engineering approach towards 3D vascularized GBM-on-chip model has been developed based on sealed microfluidic channels, endothelialized to mimic the BBB, together with a 3D bioprinted GBM model. A membrane of micrometers pores separates these two compartments, building a tissue-tissue boundary for biochemical interaction and BBB permeability measurements as a validation of barrier functionality. With the aim at reproducing the stroma structure of a GBM, two different bioinks—specific for different cell populations—were formulated and selectively printed into the open tissue compartment. Microscopy over time was performed to analyze tumor activity. Furthermore, we tested the in vitro model under µG condition, using a Random Position Machine, for assessment of biomolecular disfunctions and phenotypic alteration as a novel strategy in brain tumor therapy. Overall, the proposed GBM-on-a-chip represents an improved development in tumor-on-a-chip model as it provides a relevant strategy of constructing tumor tissue going beyond previous limitations. Besides, to the authors' knowledge, this is the first study of its kind to investigate the progression of GBM in a hybrid in vitro model under simulated µG condition and further improvements of the system will be useful for investigating the effect of mechanical unloading as a strategy for reversible enhanced drug delivery across the BBB.

2. Results

2.1. Development of the GBM-on-a-Chip

The aim of this study was to develop and characterize a new class of 3D microfluidic-bioprinted model of a vascularized GBM-on-a-chip, designed to recapitulate the pathophysiological conditions of the tumor and surrounding vascular microenvironment. In vivo GBM grows in a dense spherical shape, displaying morphologically distinct regions within the brain tumor micro-environment. This includes the necrotic tumor niche (core), where BBB integrity is highly compromised, the perivascular tumor region (intermediate) where abnormal, leaking vasculatures and tumor spheroids can formed, and the healthy adjacent brain environment where an intact BBB hampers chemotherapeutics diffusion.[56,57] To replicate this complex tumor stroma organization, we designed a custom microfluidic network and produced it by casting poly (dimethyl siloxane) (PDMS) onto a photolithography-made mold. The device consists of three independent compartments connected through two interfaces made of a series of 6×6 µm^2 pores alternating every 50 µm. Specifically, these compartments included: a) a dedicated central tissue compartment (6 mm x 100 µm, width and height, respectively, **Figure 1**A-i in red); b) a single vascular channel (200 µm x 100 µm, width and height, respectively, Figure 1A-i
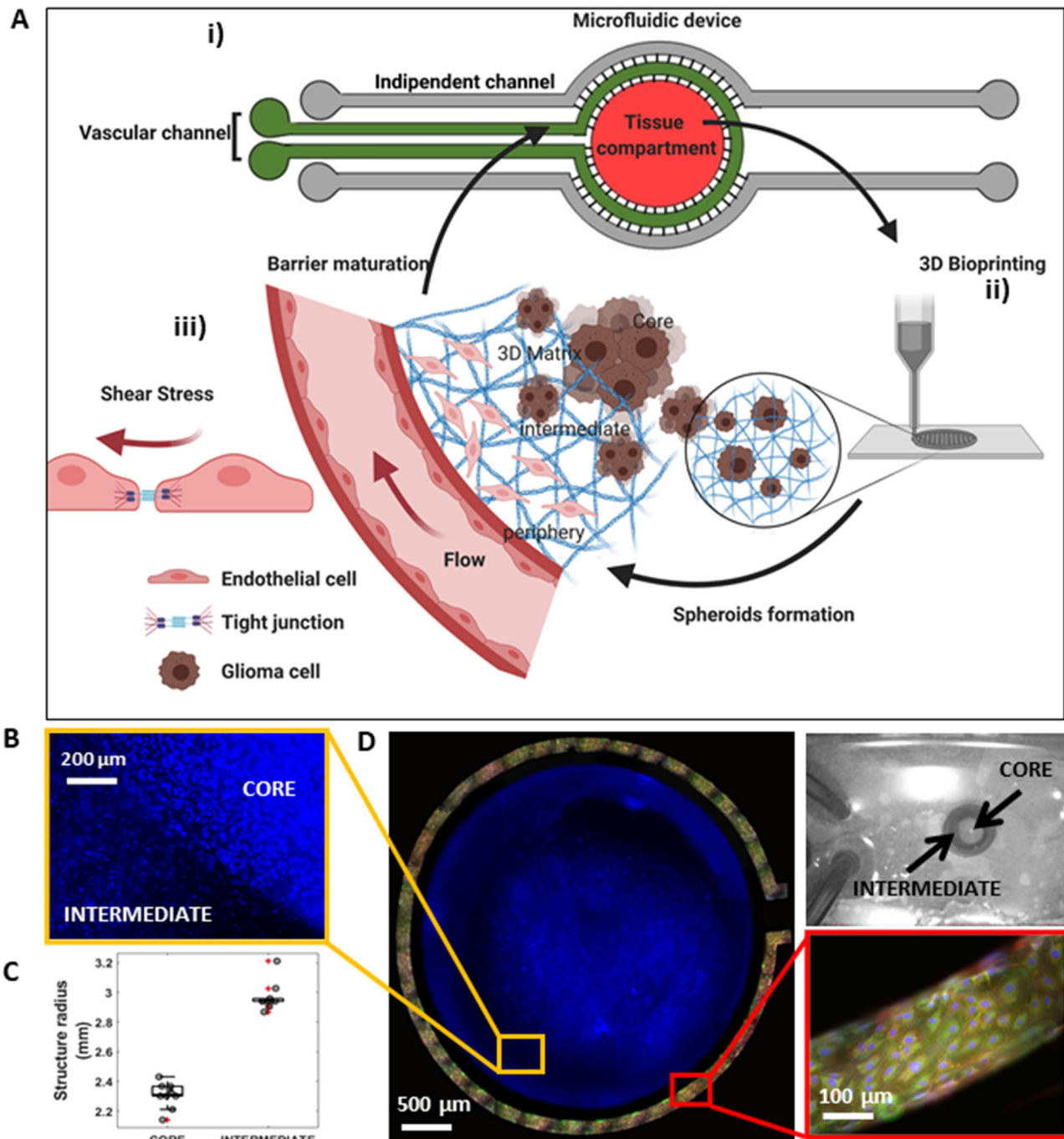
Figure 1. Vascularized GBM-on-a-chip. A) Sketch of the GBM-on-a-chip. i) Microfluidic device geometry showing the tissue compartment (red) surrounded by a circular vascular channel (green) and two independent outer channels (grey). ii) Representative bioprinting procedure for the compartmentalized tumor–stroma concentric structure. iii) Cartoon of the physiological relevant vascular feature for junction maturation, namely the shear stress. B) Fluorescence image showing nuclei of both pre-stained GBM cells and endothelial cells printed separately into the core and intermediate structures, respectively. C) Box plots and scatter data points for structure's radius analyzed for core and intermediate region. D) Fluorescence image reconstruction of the entire system comprising the GBM-loaded hydrogel and the vascular vessel all around the 3D tumor environment. Black and white picture showing the distinct regions printed into the microfluidic tissue compartment is also shown.

ADVANCED
SCIENCE NEWS
www.advancedsciencenews.com

ADVANCED
THERAPEUTICS
www.advtherap.com

in green) surrounding the tissue compartment; and c) two other independent microfluidic channels placed on either side of the device (Figure 1A-i in gray).

The open tissue compartment was created by biopsy punch to allow for direct 3D bioprinting of the tumor construct (Figure 1A-ii), comprising of highly concentrated GBM cells and surrounding brain endothelial cells. The vascular channel was coated with a layer of brain endothelial cells and subjected to the physiological shear stress of 9 dyne/cm^2 for barrier functionality maturation (Figure 1A-iii).[18,19] The outer channels were designed with the intended purpose of future application for media perfusion, drug testing and the introduction of other cell types forming the heterogeneous brain tumor environment, for example, astrocytes. Another important feature of the GBM-on-a-chip is the interconnecting porous membrane which allows for biochemical and mechanical interaction between the three different compartments thereby creating a dynamic GBM environment.

2.2. GBM Functional Behavior in a 3D Hydrogel-Based Structure

To develop a physiologically relevant GBM model, 3D bioprinted hydrogel-based constructs were used to emulate the stroma concentric structure of a GBM. To do so, we prepared two different bio-inks compositions, as explained in the experimental section. In particular, we used the commercially available blend of gelatin methacryloyl (GelMA)-Alginate to mimic the complexity of the GBM environment and improve printability of the construct, while for endothelial tissue-specific functionality we used the blend of GelMA-Fibrin. Fibrin has been proven to promote physiologic vasculogenesis and it has been extensively used for modeling tumor vasculature.[58,59] The GelMA Fibrin bioink loaded with brain endothelial cells (hCMEC/D3) was first bioprinted in a ring shape (intermediate region) and then the construct was filled centrally with GelMA-Alginate bioink (core region) loaded with GBM cells, as shown in Figure 1B. In our experiments we observed that, through photocuring, the glycoprotein fibrin provided a more favorable physiological support toward vasculogenesis processes when compared with GelMA-Alginate (Figure S1, Supporting Information). Together, these two GelMA compositions exhibited shear-thinning and fast crosslinking features, precise spatial deposition, and good dimension construct reproducibility (Figure 1C). The macro-scale dimension of the complete vascularized GBM-on-a-chip is shown in Figure 1D.

To capture the complex dynamic of GBM invasion into the surrounding brain tumor environment, constructs were printed and evaluated for tumor spheroids proliferation over time. GBM cells were cultured in growth media until 90% confluency at which point, they were stained with Hoechst nuclear stain and resuspended in the bioink to allow for fluorescence live imaging and finally printed to fulfill the ring-shape structures previously created. The entire printed construct was then cross-linked with UV light and monitored at different time points, that is, 24-, 48-, 72 h. Fluorescence microscopy immediately after bioprinting procedure revealed that GBM cells were organized mostly as single cells suspension and well confined by the surrounding 3D ring structure (**Figure 2**A). After 24 h in humidified atmosphere at 37 in 5% CO_2, cells displayed a tendency to normally form spheroids at the periphery of the core construct, as shown in Figure 2B

by the aggregated fluorescence signal of cell nuclei encircled by the red dash lines. This propensity to form spheroids was also found in,[54] although the bioink used to mimic tumor microenvironment was a fibrin-based bioink. Live imaging with Calcein-AM after 72 h of culture, also confirmed spheroids viability (Figure 2C). By inspection using ImageJ software, aggregated cells nuclei were identified around the tumor core and post-processed for quantification. A histogram averaged over 6 samples revealed that spheroids grow in number and dimension over time (Figure 2D), confirming the potential of our model to recapitulate the 3D physiological condition influencing GBM functional behavior.

2.3. Development and Characterization of the BBB Model

To establish the intact biological barrier surrounding the tumor stroma, we engineered and characterized the vascular channel of the microfluidic device with two endothelial cells line from different vascular beds, namely human umbilical vein endothelial cells (HUVECs) and human cerebral microvascular endothelial cell line (hCMEC/D3). Prior to cell seeding protocol, the microfluidic channel was functionalized using fibronectin, a glycol-protein of the extracellular matrix, favoring endothelial cells adhesion to the PDMS walls. After 72 h of culture with the perfusion of the corresponding grown media at the physiological shear stress of 9 dyne/cm^2, both endothelial cell lines organized themselves in a cylindric well packed monolayer attaching to the surrounding functionalized walls.

The applied shear force induced a mechanotransduction process followed by cells alignment in the streamwise direction. Co-localization of actin filaments and the tight-junction protein zonula occludens-1 (ZO-1) at cell–cell border were observed at the end of the culture protocol with immunofluorescence microscopy (**Figure 3**A). At this stage, ZO-1 was localized at cell periphery, showing a linear pattern along the perimeter of the cells. Along the process of junction formation, actin filaments also rearranged into cortical filaments around the periphery of the cells, as previously investigated.[57,60,61] As shown in Figure 3B, epifluorescence images of cell nuclei, corresponding to three planes at the bottom, middle, and top of the channel, respectively, also confirm that cells completely line the channel wall, resulting in a perfusable lumen. All together these observations suggested a functional biological barrier.

To quantify the permeability of the mature endothelia and capture the differences between the two vascular beds, fluorescent dyes (Dextran Texas Red, 40 kDa) was injected into the channel as schematic illustrated in Figure 3C. Due to its high molecular weight, the dextran well mimics the pharmaceutical macromolecule that fails to diffuse across the endothelial barrier. The experimental method allowed for dye diffusion observation through the porous membrane, as shown in Figure 3D. The difference in time-dependent fluorescence dye accumulation into the tissue compartment during time-lapse acquisition is reported in Figure 3E for the three separated conditions, including: without cells (in black), with HUVECs (in red) and with hCMEC/D3 (in blue). To optimize the system, the permeability of an empty device was first calculated and then subtracted from the total apparent permeability to obtain the actual permeability of
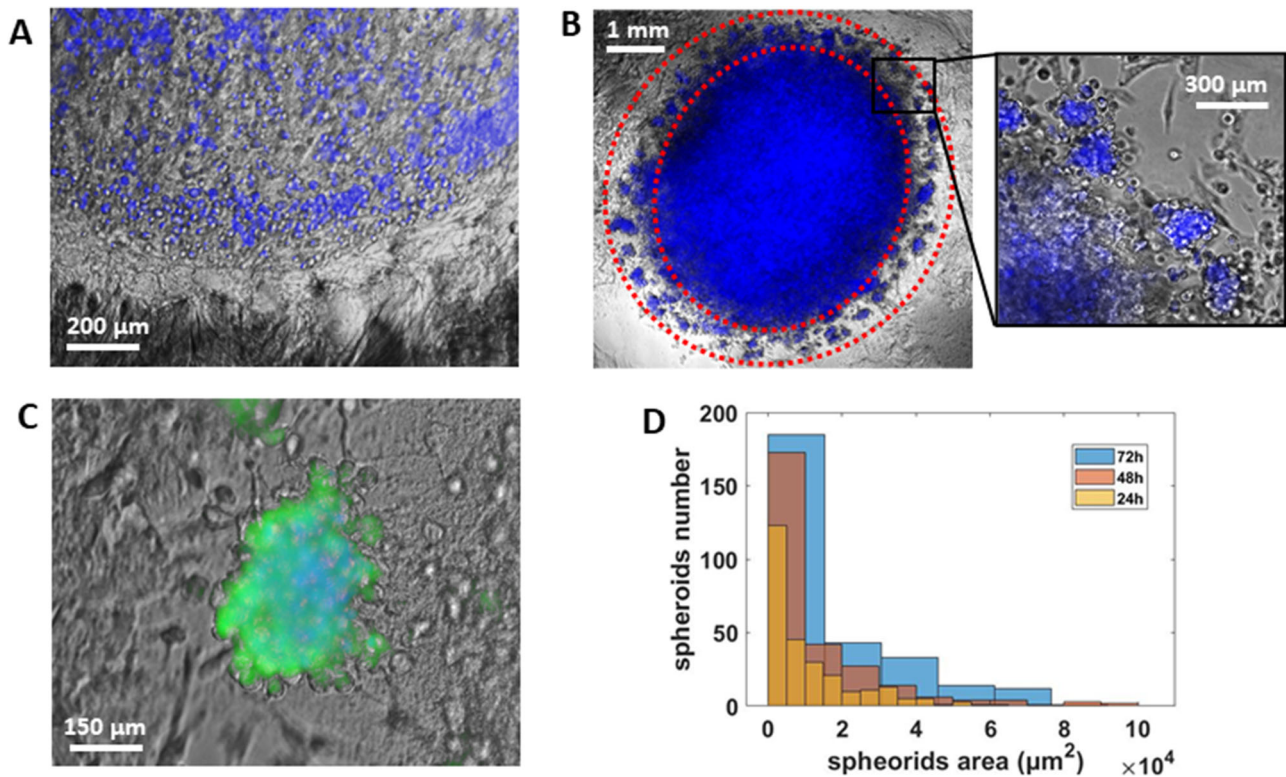
Figure 2. GBM Spheroids formation and characterization. A) Overlay of fluorescence and brightfield images showing the homogeneous distribution of GBM nuclei fluorescence signal into the core structure immediately after printing procedure. B) Overlay of fluorescence and brightfield images showing aggregated cells into spheroids at the periphery of the construct after 24 h from printing procedure. The inset highlights the spheroids around the tumor core. C) Overlay of fluorescence and brightfield images of a single spheroid. In green, fluorescence signal of live GBM cells stain with Calcein AM and in blue Hoechst signal from cells nuclei after 72 h of culture. No signal was detected from red-fluorescent ethidium homodimer-1 (EthD-1). D) Histogram showing the distribution of spheroids in number and dimension at different time, namely after 24 (yellow), 48 (orange), and 72 h (light blue) from bioprinting procedure.

the biological barrier. As the results show, there was a significant reduction over time of fluorescence dye diffusion in the presence of the cellular barrier, demonstrating that the fluorescent dextran diffusion toward the porous membrane was hampered by the formation of adherent junctions connecting neighboring endothelial cells. More interesting, endothelia cultured with hCMEC/D3 brain endothelial cells exhibited a higher dye diffusion resistance compared to HUVEC endothelia. The histogram in Figure 3F shows the mean value over the biological triplicate of the permeability coefficient for the three conditions. The results confirm that our BBB (blue) has a permeability coefficient of 1.49×10^{-5} cm s^{-1}, an order of magnitude lower than the endothelium formed by HUVEC (red), that is, 1.13×10^{-4} cm s^{-1}, in line with previous outcome of BBB permeability measurements.[62–66]

2.4. Impact of Microgravity at the Cellular Level

As a first step toward understanding the effects of simulated microgravity (µG) on GBM functionality in a 3D environment, we subjected the bio-printed tumor constructs to 72 h of µG condition. Immediately after bioprinting procedures, with a GBM distribution as single cells, the models were placed on the Random Position Machine (RPM) inside the incubator. The

system achieves microgravity by continually providing random changes in orientation relative to the gravity vector, allowing the cells behaving as they were in space thus adapting to the new environment.

Interestingly, the results show that the absence of the gravity field inhibits GBM cell invasion and aggregation into the surrounding microenvironment. Inset in **Figure 4**A highlights the periphery of the GBM core under native gravity condition were cells preferentially formed spheroids. Live imaging with Calcein-AM also confirmed spheroids viability, as previously captured during characterization of our tumor model. On the other hand, GBM cells remained homogeneously distributed and confined into the tumor core at the end of the µG assay, as shown in the inset of Figure 4B. Although GBM cells appear to be alive, with a strong Calcein-AM fluorescence signal after 72 h of mechanical unloading and an absent signal from red-fluorescent ethidium homodimer-1 (EthD-1), their aggregation activity remained suppressed. These findings demonstrated that GBM spheroids formation is gravity dependent, and, in its absence, µG compromises GBM basic cell function and mechanisms.

To further investigate on the impact of µG on biomolecular disfunctions and phenotypic alteration of the GBM model, Human Glioblastoma A-172 and hCMEC/D3 were seeded into conventional 2D plate, exposed to 24 and 48 h of µG, and subsequently
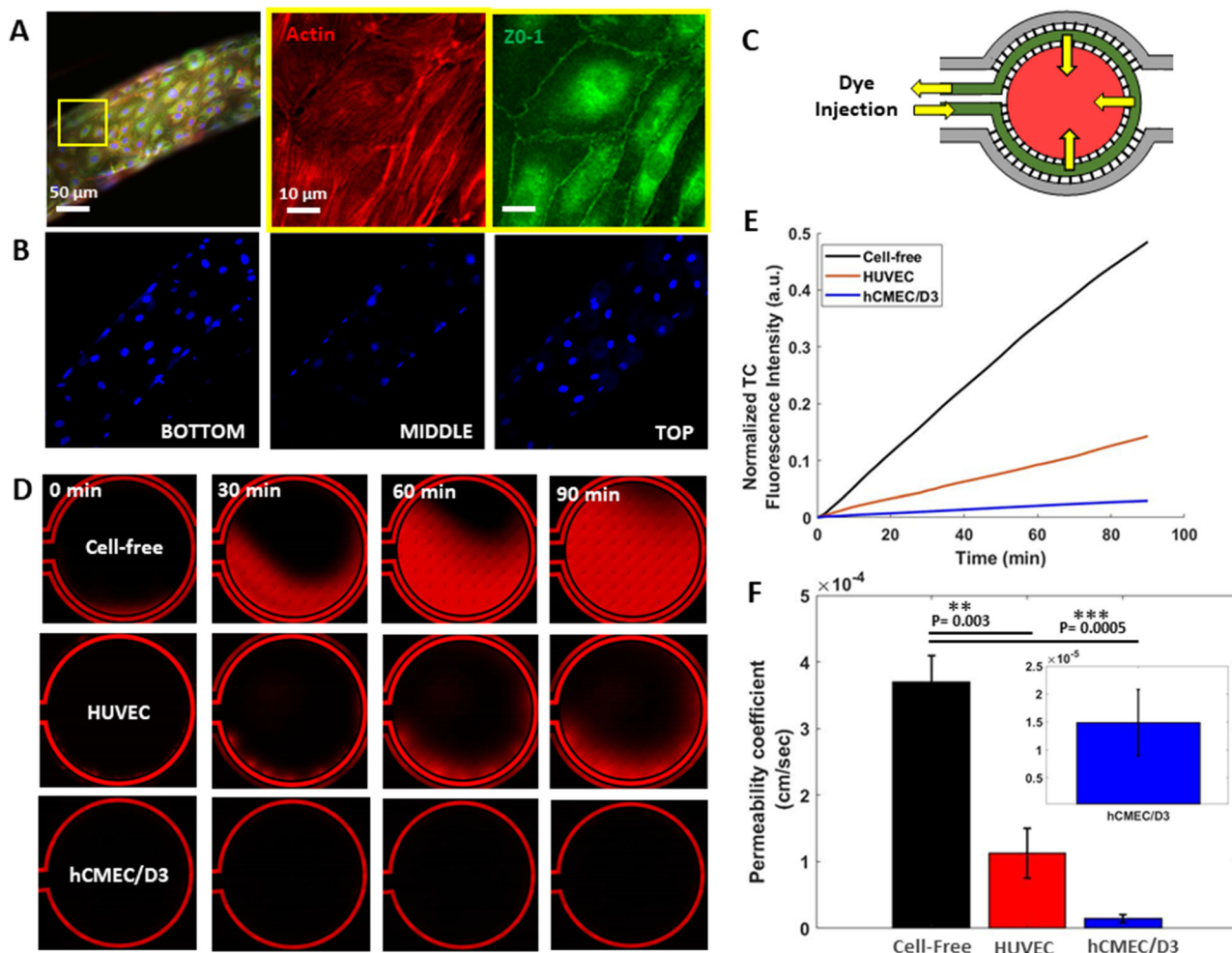
Figure 3. BBB model characterization. A) Overlay of wide-field fluorescence image showing cell nuclei (blue), actin filaments (red), and ZO-1 junction proteins (green) of the vascular channel cultured with HUVECs cells. B) Fluorescence images of cell nuclei at the bottom (left panel), middle (central panel), and top (right panel) sections of the vascular channel. C) Sketch of the permeability assay procedure. D) Representative images of fluorescence dye diffusion into the tissue compartment at different stage of the time-lapse. E) Comparison of normalized tissue compartment fluorescence intensity in a cell-free device (black curve), HUVECs-covered device (red curve), and hCMEC/D3-covered device (blue curve) for a single experiment. F) Histogram showing permeability coefficient comparison. Data are shown as the mean ± SEM ($n = 3$). *P*-value is reported for statistical significance.
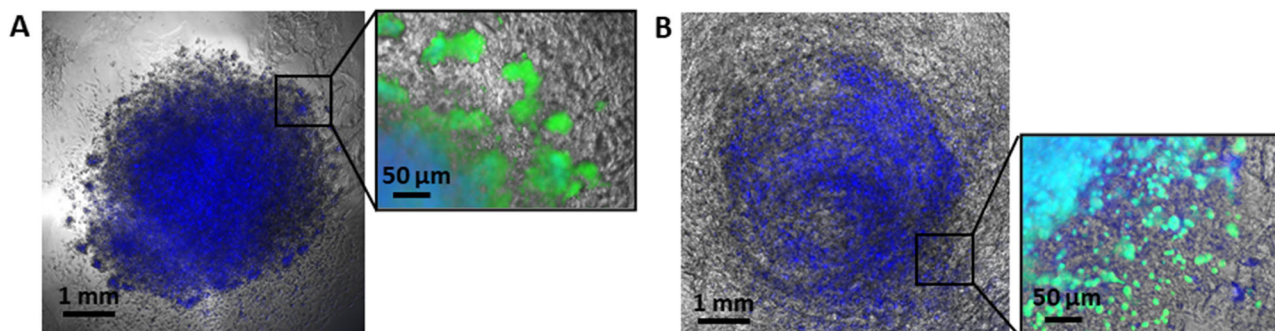
Figure 4. Microgravity(μG)-induced inhibition of tumor spheroid formation. Overlay of fluorescence and brightfield images showing aggregated cells into spheroids at the periphery of the construct after 72 h of native gravity (A) and μG (B) condition. Inset shows live cell imaging of GBM cells around the tumor core stain with Calcein AM (green) and Hoechst signal from cells nuclei (blue) at the end of μG assay. No signal was detected from red-fluorescent ethidium homodimer-1 (EthD-1).
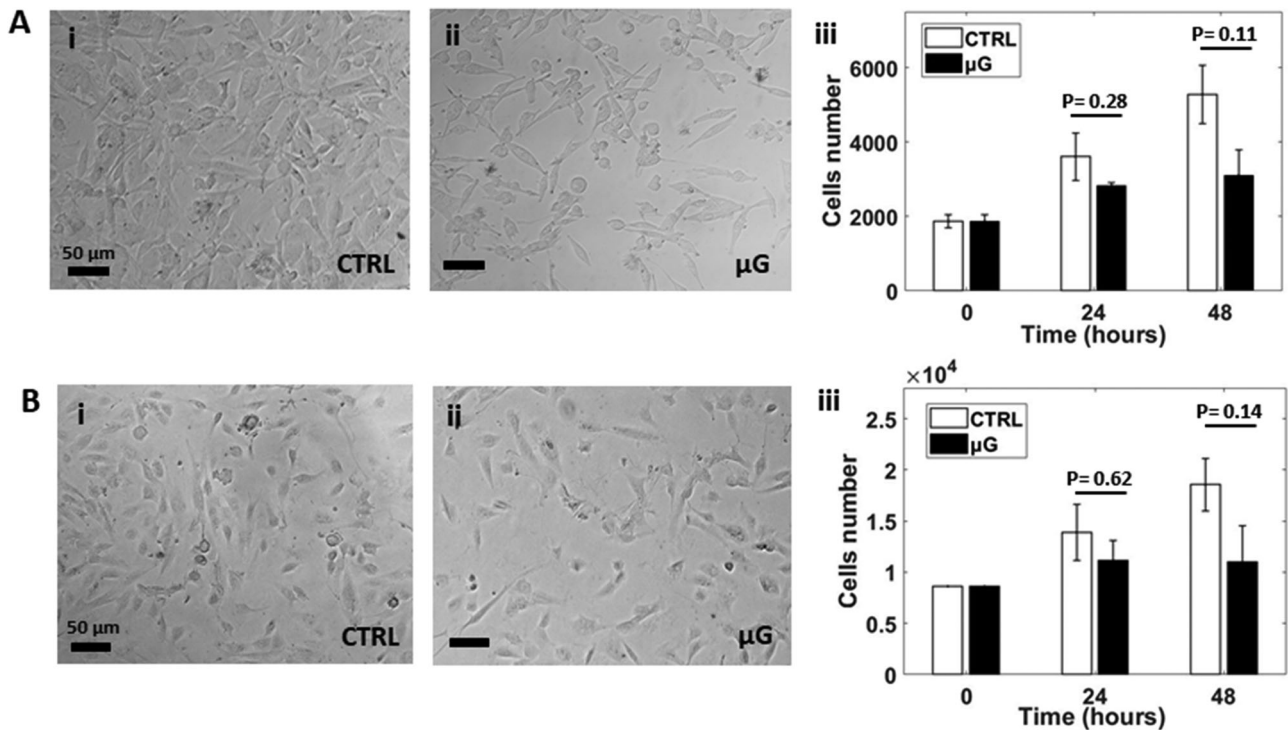
Figure 5. µG effects on cell proliferation rate. Brightfield images of GBM (A) and hCMEC/D3 (B) cells after 48 h under control (i) and µG condition (ii). (iii) Cell proliferation assay for cells at different time points and experimental condition, namely after an overnight, 24- and 48 h from seeding procedure, exposed or not to µG conditions. Data are shown as the mean ± SEM (*n* = 3). *P*-value is also reported.
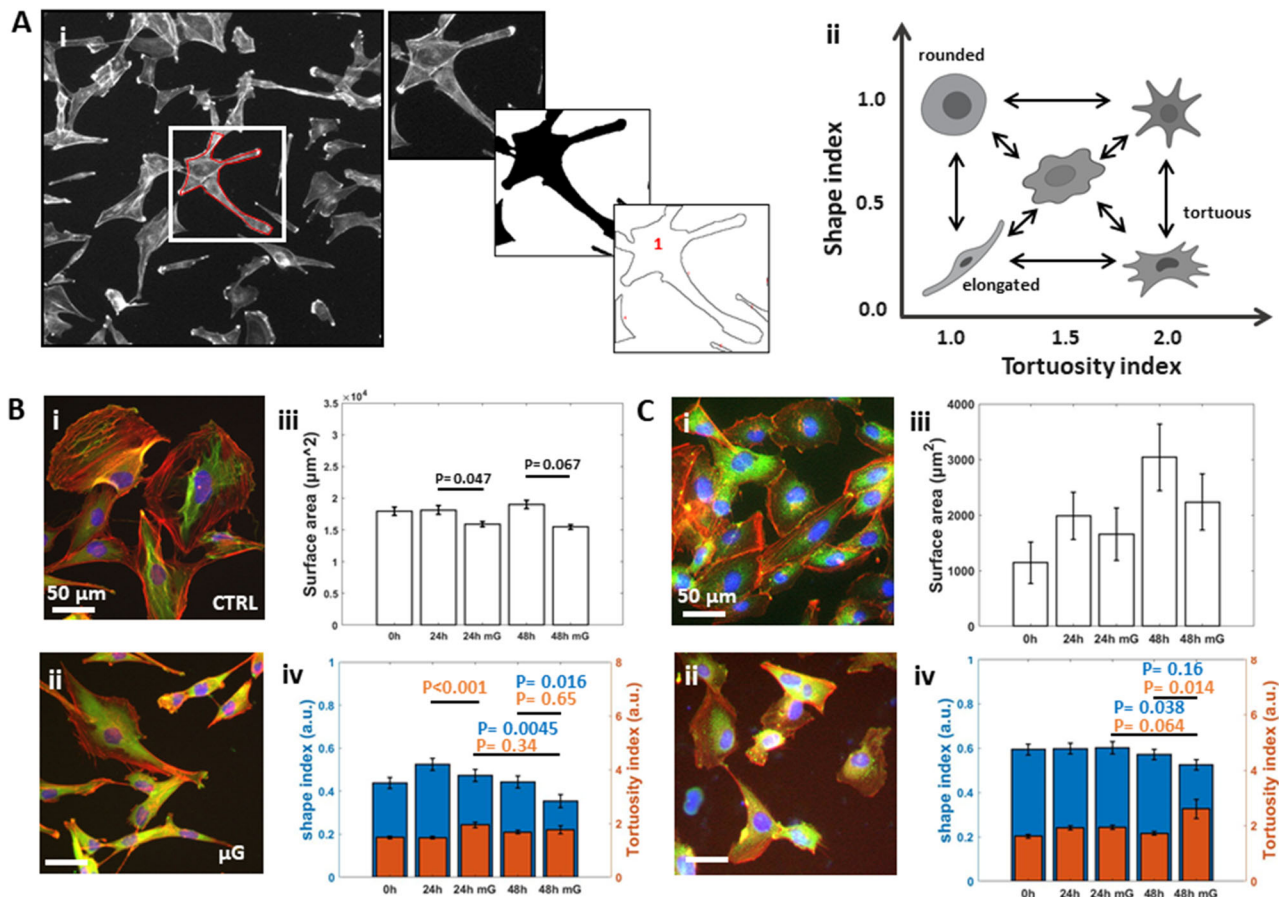
characterized. Examination of cells proliferation rate, as shown in **Figure 5**A,B, demonstrated that µG induced inhibition of GBM growth, with hCMEC/D3 showing similar trends.

Quantitative analysis for morphology changes under µG exposure was performed on fluorescence images. Briefly, the cell outline was manually extracted using ImageJ software by selecting the peripheral actin filaments (**Figure 6**A-i) and a binary image was created and used for automatic quantification of morphology parameters, such as cell surface area, shape index (SI), and cell perimeter. The SI value is a measurement of cell roundness, from a perfect spherical shape (SI = 1) to an elongated shape (SI = 0). Another parameter, known as tortuosity index (TI), assesses and quantifies whether cell approaches a smooth circular or elliptical profile (TI = 1) or an irregular star shape profile (TI >1). A sketch of the relationship between the shape, the tortuosity index, and the corresponding morphological changes is illustrated in Figure 6A-ii. With this in mind, the results obtained from the GBM cells exposed to 24 and 48 h of µG (Figure 6B-i,ii) show a significant change in cell surface area compared with the respective control (Figure 6B-iii). Moreover, GBM became more elongated at the end of the µG assay (Figure 6B-iv, blue) while maintaining a tortuous profile in the range of TI = 0.1–0.3 (Figure 6B-iv, red). hCMEC/D3 cells showed a different behavior under the effect of µG (Figure 6C-i,ii). Along with the natural tendency of endothelial cells to grow and assume the shape of elongated polygons, the cells changed in surface area after the exposure of µG (Figure 6C-iii). Similar trend has been found for HUVECs, although more pronounced with a decreasing in surface area by 49% for 24 h µG exposure, and 88% for 48 h compared to control (Figure S2,

Supporting Information). While maintaining the SI in the range of 0.65–0.55 (Figure 6C-iv, blue), hCMEC/D3 cells shown a significant increase of the TI by the 34% at the end of the µG assay (Figure 6C-iv, red). These results demonstrate that cell morphology regulation is gravity dependent thus supporting the role and impact that µG can have on GBM tumor phenotype.

In-cell western blotting method was also used to investigate on proteins expression for GBM and hCMEC/D3 cells. GBM cells were stained for vinculin and active Yap1 proteins. Vinculin is important in cell migration and adhesion processes as one of the main proteins involved in anchoring the actin cytoskeleton to the integrins of the ECM and transmitting mechanical signals.[67] While following the same gravity expression level after 24 h of µG exposure, GBM cells exposed to 48 h of µG shown a 47% decrease of vinculin expression compared to control (**Figure 7**A). Active Yap1 is a protein directly involved in cell proliferation mechanism, acting as a transcriptional regulator.[68] In line with the results obtained by cell proliferation assay, we found that Yap1 protein in GBM cells decreased by 17% after 24 h, and by 55% after 48 h compared to the level of protein expression under normal gravity (Figure 7A). Yap1 protein is also known to be an important molecule in mechanical signaling pathways that control endothelial activation and vascular inflammation.[69,70] For this reason, we also examined the level of Yap1 expression in hCMEC/D3 cells and we found that this protein responded to the exposure of µG only after 48 h with a decrease of the 32% compared to control (Figure 7B). Finally, Figure 7B shows the expression of the tight junction protein ZO-1 in hCMEC/D3. As Yap1 protein, also the expression of ZO-1 proteins was compromised only after 48 h

**ADVANCED
SCIENCE NEWS**

www.advancedsciencenews.com

**ADVANCED
THERAPEUTICS**

www.advtherap.com

Figure 6. µG -induced alteration of cell morphology. A) Schematic representation of morphology analysis method. i) After cell outline identification, a binary image was created, and morphology parameters of the figure obtained were found automatically using analyze particle in ImageJ software. ii) Relationship between the shape and the tortuosity index. B) Overlay of wide-field fluorescence images showing cell nuclei (blue), actin filaments (red), and vinculin proteins (green) of GBM cells under 48 h of gravity (i) and µG (ii) condition. iii,iv) Bar plots showing the time course changes of surface area (white), Shape Index (blue), and Tortuosity index (red) after 24- and 48 h of gravity and µG exposures. C) Overlay of wide-field fluorescence images showing cell nuclei (blue), actin filaments(red), and ZO-1 junction proteins (green) of hCMEC/D3 cells, under 48 h of gravity (i) and µG (ii) condition. iii,iv) Bar plots showing the time course changes of surface area, Shape Index, and Tortuosity Index. *P*-value is reported for statistical significance.

of µG condition with a decrease of the 37% compared to control. This suggests that a lack of gravity may induce detrimental effects on vascular integrity by hindering junction formation at cell–cell border, as previously hypothesized.

3. Discussion

Despite continuous effort in developing an effective chemotherapeutic strategy, GBM remains incurable, resulting in high rates of recurrence which is the primary cause of death. This is partly due to the high grade of dynamic GBM invasion within the surrounding brain tumor microenvironment and to the lack of successful drug delivery across the BBB. Healthy BBB are highly selective in solute transport across the barrier in order to protect the central nervous system from potentially harmful elements present in the blood.[71] This is mainly due to the presence of tight junctions between brain endothelial cells lining the vessel wall, which are regulated by the dynamic interaction with actin filaments of the cytoskeleton in response to fluid mechanical stress exerted by the blood flowing upon their apical surface.[18] In pathological con-

ditions, including GBM, the BBB is heterogeneously disrupted and is characterized by changes to endothelial morphology, non-uniform permeability, and dysfunctional solute transport.[71,72] Importantly, although highly compromised within the necrotic tumor core, an intact and functioning BBB is present within the healthy adjacent brain tumor environment causing a limited and ineffective access of drug to tumor cells.[23,73] Thus, a potential approach to overcome the low access of chemotherapeutics to tumor cells has become the major challenge in GBM drug delivery.

To examine the GBM tumor progression and investigate the interplay between the GBM with the surrounding microvascular network, several in vitro platforms have been engineered, including microfluidic devices and 3D cell-laden hydrogel scaffolds.[74–76] However, there is still a lack of a physiologically relevant and equally advanced cellular model to recapitulate the complex brain tumor environment, which includes a functional vascularization and a 3D compartmentalized structure of the tumor itself. For instance, the system proposed by Truong's team provides a biomimetic brain microenvironment by integrating hydrogel-based biomaterial in a microfluidic device

**ADVANCED
SCIENCE NEWS**
www.advancedsciencenews.com

**ADVANCED
THERAPEUTICS**
www.advtherap.com
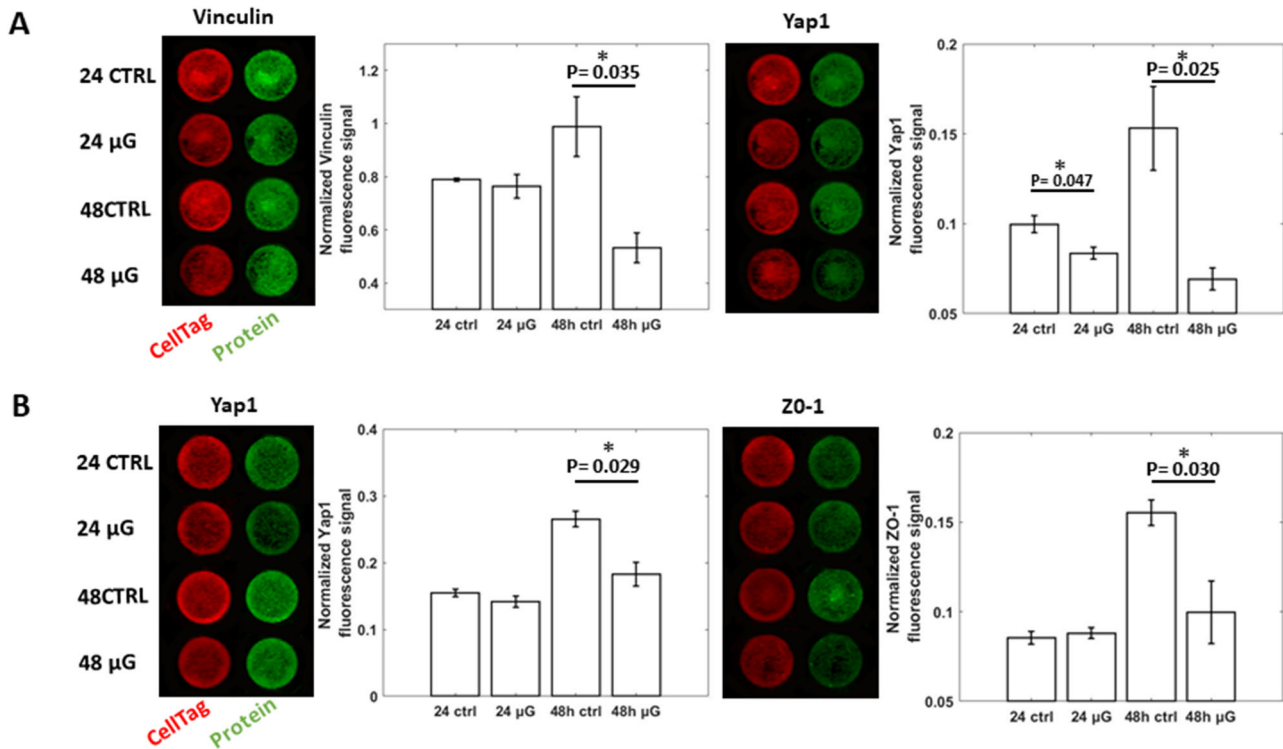
Figure 7. Impact of μG on protein expression levels. A) In-cell western blot assay of the changes in Vinculin and Active Yap1 proteins expression levels of GBM cells in response to 24 and 48 h of microgravity exposure. B) In-cell western blot assay of the changes in active Yap1 and ZO-1 proteins expression levels of hCMEC/D3 cells in response to 24 and 48 h of microgravity exposure. Data are shown as the mean ± SEM ($n = 3$). *P*-value is reported for statistical significance.

to mimic the GBM microvascular network and investigate on the influence of endothelial cell on tumor invasion.[44] In another study, Yi's team developed a 3D bioprinted brain tumor model for testing patient-specific chemotherapeutic treatments.[55] By recapitulating important physiological features of GBM, such as the hypoxic tumor core characterized by a radial oxygen gradient, Yi's group was able to establish the peculiar structure of the native brain tumor environment, including endothelial cells in the peripheral region of the tumor core. Han and collaborators realized an in vitro screening system for anti-cancer drugs, by printing a blood vessel layer consisting of multicellular architecture, followed by seeding pre-established GBM spheroids onto the blood vessel layer.[77] Although sophisticated, all these models lack in mimicking the physiological fluid mechanical stimulus from the blood shear stress, which is known to be essential for endothelial functionality.[18,19] As such, in the absence of the mechanical interplay from physiological fluid flow, the aforementioned systems are not suitable for developing future drug delivery strategies.

In a more recent study, Tricinci team proposed a real-scale 3D-printed microfluidic device able to replicate the blood neovasculature exploiting two-photon lithography (TPL) technology.[78] Their platform demonstrates to be suitable for high-throughput drug screening for brain cancer therapy, allowing for the interaction of different tissues. However, the soft 3D environment surrounding and supporting the cells is missing and the self-organization into physiological architecture, emulating that of the native tumor microenvironment, is negate.

The hybrid vascularized GBM-on-a-chip described in this study was developed with the synergy of microfluidic and bioprinting technologies by simultaneously recapitulate important physiological features of in vivo GBM, such as flow shear stress and cell–matrix mechanical interaction which addresses many of the technical challenges towards a more biomimetic in vitro tumor model. Firstly, by bioprinting GBM cells in bioinks as opposed to pre-formed tumor spheroids, facilitates the ability to detect and monitor the GBM self-structural organization and the dynamic activity of tumor on-set and progression with/without μG condition. Moreover, 3D bioprinting technology allows the user to selectively embed different cell types in specific engineered hydrogels with selected stiffness. In addition, the sealed microfluidic channel allows for controlled perfusion at the physiological flow rate for BBB maturation and drug injection. Owing to the optical properties of PDMS and the confined intact vasculature, microscopy observation and analysis of junction proteins can be performed with high resolution microscopy including confocal microscopy, providing insight in vascular cell mechanotransduction and permeability at junction level. Finally, the hydrogel construct into the open tissue chamber can be easily collected at the end of the μG experiment, allowing for gene expression analysis of cells cultured in a 3D environment. Here, taking advantage from the control over spatial deposition of different bioink composition, we obtain precise co-localization of heterogeneous cell population. The spontaneous transition of GBM cells into aggregated cells spheroids confirmed the feasibility of the system to recapitulate the physiological 3D organization

**ADVANCED
SCIENCE NEWS**
www.advancedsciencenews.com

**ADVANCED
THERAPEUTICS**
www.advtherap.com

of a functional GBM, when bioprinted within the bioink. The system was also able to capture the differences of vessels from different vascular beds, although it lacks support stroma cells forming the heterogeneous brain tumor environment, such as astrocytes and pericytes. For this purpose, two independent outer channels, along the perimeter of the vascular channel have been designed for further improvements of the system adding higher levels of complexity to our tumor model. It should be noted that the GBM tumor was only bioprinted after having assessed the biological barrier functionality to avoid artificial morphological alteration of the endothelium during maturation due to the close proximity of the tumor. However, observation of the vasculature after bioprinting the GBM tumor revealed that during overnight, tight junctions at cell–cell border were compromised (Figure S3, Supporting Information). This result indicates a biochemical interaction across the BBB and GBM tumor boundary and future studies will examine the biology of this interaction. Taken together, the GBM-on-chip has demonstrated to provide a more biomimetic approach towards a more realistic GBM tumor model offering the flexibility to allow for future expansion and modification.

To evaluate the tumor response to the external unbalanced of forces, the bioprinted model was exposed to simulated μG using a Random position machine. In line with studies showing the significant impact that μG has on tumorigenesis, specifically on cancer cell mechanotransduction,[27] our results supported the gravity dependency of GBM's susceptibility. When the 3D bioprinted GBM tumor was exposed to three days of μG, the spontaneous aggregation of GBM cells into the surrounding microenvironment was inhibited, remaining homogeneously distributed inside the tumor construct. Conversely, under native gravity condition, GBM cells spontaneously aggregate in spheroids. These findings may suggest that the initial formation of GBM tumor is based on gravity-driven mechanotransduction and that the lack of gravity can compromise and disrupt GBM cell's function and mechanisms. Further examination, that is, cell proliferation, morphological aspect, and proteins expression confirmed that even in a 2D environment, the GBM and brain endothelial cells are able to "sense" microgravity and respond to these low emitting forces. Conducting these experiments in 2D provides results comparable with other established studies as 3D culture studies are still limited and technically challenging for elucidating cell mechanotransduction. Future studies will compare and identify the changes in cell properties in both 2D and 3D environment.

The changes in actin cytoskeletal structure naturally pointed to changes in cell focal adhesion. Vinculin protein expression in GBM cells showed significant reduction after 48 h of μG exposure which is consistent with cell morphological changes and indicates that the cells are starting to lose their adhesion. Studies in human breast cancer cells[79] and Mesenchymal stem cells[80] have shown similar observation under μG in which focal adhesion expression was reduced. One of the most known mechanotransduction pathways preserved in cancer is the Hippo-YAP pathway which regulates cancer cell function and survival.[81,82] Active YAP protein expression in the GBM cells was significantly reduced already within 24 h and even more at 48 h as opposed to the control group in which YAP expression was increasing at 48 h. Together these findings support our hypothesis that exposure to a "lack of gravitational forces" inhibits GBM cell mechanotransduction processes, as the cells lose

their adhesion and proliferation ability thus resulting in a suppression of cells migration and aggregation towards spheroids formation. Regarding Active YAP protein expression in brain endothelial cells, our results showed a delay in responding to a lack of gravity, reaffirming that cells respond differently to different mechanical stimuli. Finally, the reduction in tight junction protein ZO-1 expression in brain endothelial cell after exposure to μG demonstrated that mechanotransduction plays an important role in vascular integrity. Tight junctions are essential for controlling vascular physiology and the lack of ZO-1 expression after 48 h of μG condition may suggest an increase in cell permeability with a dysregulated barrier functionality. Similar results were found by Alvarez et al. revealing that epithelial barrier undergoes sustained disruption upon removal of μG environment. This is a significant finding as this demonstrates that μG studies combined with the GBM-on-the-chip can represent a new approach towards addressing the challenge in ensuring the delivery of effective concentration across the BBB of chemotherapeutics. Future studies will focus on unlocking the molecular mechanisms that regulate and dysregulate endothelial barrier integrity in a GBM context to develop novel therapies that specifically target GBM vascularization to halt the progression of this deadly disease.

4. Conclusion

This study fills the gap between current in vitro platforms for brain cancer therapy by establishing an innovative 3D vascularized GBM system with dynamic flow and volumetric cues. The platform displayed accurate recapitulation of GBM tumor environment and further development will allow for studies on cell–cell interaction in brain tumor pathophysiology condition. Moreover, the model responded to the lack of gravity by compromising GBM tumor mechanics and BBB function. This demonstrates that our system provides a biologically relevant platform for revealing insights of GBM mechanobiology under mechanical unloaded condition, as well as the potential development of a strategy for drug delivery across the BBB.

5. Experimental Section

Microfluidic Device Fabrication: The microfluidic device was manufactured by replica molding blending PDMS and cross-linker at a ratio of 10:1 and curing the degassed mixture in a SU-8 master mold at 70 °C for a minimum of 2 h. The SU-8 mold was specifically designed for the experiment using CAD software and realized with soft lithography process. The design (refer to sketch in Figure 1) consists of a central tissue compartment (6000 μm width, 100 μm height) encircled by a vascular channel (200 μm width, 100 μm height) and two independent outer channels (200 μm width, 100 μm height). The vascular channel communicates on both sides with the outer channels and the tissue compartment through two interfaces made of a series of 6×6 μm^2 pores alternating each 50 μm. After PDMS polymerization, devices were peeled off the mold and cut to separate each device. The inlets and outlets holes were punched before the device was plasma bonded to a microscope glass slide. Using a 6 mm puncher, a hole was also created in the tissue compartment and the opened macroscale chamber allowed for controlled cells-loaded hydrogel deposition using a commercialized 3D bioprinter (Bio X TM, Cellink). The sealed microscale channels were functionalized with endothelial cells and perfused with growing media at the physiological flow rate of 9 dyne/cm^2, mimicking the BBB found in vivo.[18,19,64,83] For permeability experiments, the tissue compartment was not punched to avoid light scattering due to the fluorescence molecule diffusion and accumulation in the bigger volume.

Cell Culture: Human Glioblastoma cells A-172 were purchased from Sigma (Cat. No. 88 062 428), cultured with high-glucose Dulbecco's Modified Eagle Medium (DMEM) (Thermo Fisher, Cat. No. 11 965 084) supplemented with 10% FBS and 5% penicillin-Streptomycin (Thermo Fisher, Cat. No. 15 140 122) and kept in humidified environment at 37 °C with 5% CO_2. Media was changed every 3–4 days and cells were passaged continuously upon reaching 90–95% confluence.

HUVECs were purchased from Lonza (Cat. No. CC-2517) while cerebral micro-vessel endothelial cells (hCMEC/D3) were purchased from Sigma Aldrich (Cat. No. SCC066). HUVEC were grown in humidified atmosphere at 37 °C and 5% CO_2 using basal medium-2 (EBM-2) supplemented with endothelial growth medium (EGM-2) BulletKit from Lonza (Cat. No. CC-3162). To ensure the expression of key endothelial proteins, all experiments used cells between passage numbers 2–5. hCMEC/D3 were cultured in collagen coated flasks (Collagen Type I 1:20 diluted in PBS) using EndoGRO-MV complete culture media kit (Sigma Aldrich, Cat. No. SCME004), supplemented with 1 ng mL^{-1} of hFGF (Lonza, Cat. No. CC-4068) and 5% penicillin-Streptomycin.

Cell Seeding Into the Microfluidic Device: The procedure to seed the vascular channels with endothelial cells was adapted from[41] and here described in detail. 10^8 cells mL^{-1}.

Prior to cell seeding, the device was degassed and using Tygon tubing (John Morris Scientific, Cat. NO ND-100-80) the device washed with PBS and functionalized with 100 µg mL^{-1} fibronectin (Sigma-Aldrich, Cat. No F1141). Endothelial cells (10^8 cells/mL) were injected into the vascular channels via Tygon tubing. Once the cells have reached the desire confluency (70%) inside the vascular channel, outlet and inlet were clamped, and the device was placed in the incubator for 2 h to let the cells bind the fibronectin and attach to the channel inner wall in static condition. After incubation, each inlet tubing was immersed in a reservoir of culture medium placed inside the incubator. The outlets of each vascular channel were connected to an empty syringe and mounted on a double syringe pump (AdeLab Scientific, Cat. No. Ne4000), which was also placed inside the incubator. To orient the cells and reach the full maturation of cell–cell junctions' protein, growth medium was pulled into the channel for 72 h consecutively with a programmed ramp up. A flow rate of 0.8 µL min^{-1} (corresponding to a shear stress of 0.36 dyne/cm^2) was initially set for 16 h, followed by 2.5 µL min^{-1} for 1 h, 5 µL min^{-1} for 3 h, 7 µL min^{-1} for 6 h, 10 µL min^{-1} for 10 h, and 20 µL min^{-1} for 10 h more (corresponding to a shear stress of 1.15–2.34–3.2–4.6–9 dyne/cm^2). After the first overnight, the culture medium inside the reservoirs was refilled. The average wall shear stress associated with the flow rate applied was calculated using the following equation:

$$\tau = 6 \frac{Q\mu}{wh^2} \tag{1}$$

with the shear stress τ in dyne/cm^2, Q the flow rate in µm^3 s^{-1}, μ the dynamic viscosity in Pa s, and w and h the width and height of the channel in micrometer.

For the development of the complete tumor model, prior to endothelial cell seeding into the vascular channel, the device was punched using a 6 mm puncher to create the macro-scale compartment subsequently filled with GBM-loaded hydrogel. The compartment was then filled with media and the same dynamic culture protocol for endothelial cells was followed. At the end of the BBB formation (72 h), the media was removed from the opened compartment and the GBM model was printed as explained below.

Vascular Permeability Assay: The experimental method used to quantify the permeability of the artificial endothelial barrier is here described. At the end of the long-term cells culture protocol into the vascular channel, the microfluidic device was disconnected from the syringe pump and the inlet of the vascular channel was connected to a 1 mL syringe filled with a fluorescent dye (Texas Red-dextran 40 kDa, Thermo Fisher Scientific, 10% diluted in culture medium, starting from a stock concentration of 10 mg mL^{-1}). The fluorescence dye was then injected into the vascular channel at a flow rate of 1 µL min^{-1} and monitored under the microscope (Delta Vision Elite, GE Healthcare). As the fluorescent dextran accumulated in the central tissue compartment in a time-dependent manner,

its permeability across the endothelial monolayer was estimated thanks to a time-lapse acquisition over 1.5 h with an exposure time of 100 ms, 10% power, with a frame rate of 1 image each 2 min. Given the macro dimension of the tissue compartment, the evolution of the fluorescence signal was detected by scanning the sample with a 10× magnification objective in x–y plane for a duration of 1.2 min. The reconstruction of the entire microfluidic device was then obtained, and post processed with ImageJ and Matlab software. To quantify the permeability (P) the authors used the following equation:

$$P = \frac{1}{I_0} \frac{V}{S} \frac{dI_t}{dt} \tag{2}$$

where I_t is the average intensity in the tissue compartment, I_0 is the maximum fluorescence intensity of the vascular channel and V/S is the ratio of tissue compartment volume to the lateral diffusion surface area. The permeability of an empty device ($\frac{1}{P_{cell-free}}$) was then subtracted from the total apparent permeability (1/P) to obtain the actual permeability of the biological barrier, in analogy with parallel resistors in electrical circuits.

$$\frac{1}{P_{BBB}} = \frac{1}{P} - \frac{1}{P_{cell-free}} \tag{3}$$

The calculation of permeability was performed considering the intensity of the vascular channel saturated to a constant value. For this reason, before starting the time-lapse, the fluorescence dye was injected for 16 min corresponding to the time necessary to reach saturation.

Preparation of the Hydrogel-Embedding GBM Environment and 3D Bioprinting Procedures: To print the GBM-on-a-chip, the authors prepared two different bio-inks composition: GBM-cell-loaded GelMA-Alginate (CELLINK, Cat. No. IK352102) and hCMEC/D3-loaded GelMA-Fibrin (CELLINK, Cat. No. IKG106L3030-M). Cells were collected and resuspended in culture medium at an average concentration of 8×10^6 cells in 50 µL of DMEM and transferred into a 1.5 ml Eppendorf. A 10% gelatin-based bioink GelMA-A (w/w) (CELLINK Cat. No. IK305102) was prepared by preheating the cartridge to 35 °C to liquify the GelMA-A and bioink was then mixed with GBM cell suspension (10:1). Same procedure was followed for hCMEC/D3 embedded in GelMa-Fibrin at a concentration of 6×10^6 cells in 50 µL of EGM-2 and transferred in a new ink cartridge and placed on the pneumatic print head.

To recreate the GBM environment, the two different cell-loaded bio inks were selectively printed in 96-well plates and into the central microfluidic compartment. Specifically, hCMEC/D3-loaded GelMA-Fibrin bioink was first extruded at a pressure of 40 kPa in a ring shape at the speed of 5 mm s^{-1}, at 26 °C, and using 25G Needle. GBM-cell-loaded GelMA-A bioink was then deposited to fill the space inside the ring shape at a pressure of 80 kPa for 2 s at 28 °C. The entire printed construct was cross-linked using UV light for 5 min at 5 cm distance and 100 µL of DMEM were added into the well to keep the hydrogel hydrated. Only 70 µL of DMEM were enough to fill the tissue compartment of the device, which was closed with a glass cover slip. The sample was then kept at humidified atmosphere at 37 °C in 5% CO_2 for 4 days for experimental evaluation at different time points, namely 24-, 48-, and 72 h from printing procedures.

Microgravity Assays: A Random Position Machine (RPM) was used to simulate the microgravity condition experience in space. The system was a desktop-size 3D clinostat and works by inducing random changes to the gravity vector orientation, thus resulting in an average gravity zero vector over time. The system was used to investigate on: 1) the proliferation rate cell; 2) morphological changes; and 3) protein expression, of Human Glioblastoma A-172, HUVECs, and hCMEC/D3 in conventional 2D well plates. Also, the assay was performed for evaluation of GBM spheroids formation in the 3D-printed microenvironment. Briefly, cells were seeded into 96-well plates at a concentration of 5×10^3 cells/mL and maintained in humidified atmosphere at 37 C in 5% CO_2. After overnight incubation, plates were fulfilled with the appropriate medium and custom-made 3D printed plastic lids were positioned on top of each well. Plates were then mounted on the RPM system and two different times were investigated,

such as 24 and 48 h during microgravity exposure. For spheroids formation evaluation, 9 constructs were printed into 96-well plates and placed on the RPM system and monitored for 72 h.

Proliferation Assay: The proliferation activity of all cells was determined using CyQUANT Cell Proliferation Assay Kit (Thermofisher, Cat. No. C7026) as per manufactures instructions. Briefly, the medium was removed from each well, cells were washed with PBS and stored at −80 C until quantification. Component A and B were added to each well, incubated at RT for 5 min and the fluorescence signal read using 480 nm excitation and 520 nm emission (Tecan Life Infinite 200 PRO). A reference standard curve was generated for each cell type.

Fluorescence Staining Protocols: To assess viability of Human Glioblastoma A-172 spheroids printed either into the microfluidic compartment or the multi wells plates, live imaging using LIVE/DEAD Viability/Cytotoxicity Kit (Sigma-Aldrich, Cat. No. L3224). To discriminate live from dead cells, the constructs were simultaneously staining with green-fluorescent calcein-AM (2 µM solution) and red-fluorescent ethidium homodimer-1 (EthD-1) (4 µM solution) for evaluation of intracellular esterase activity and loss of plasma membrane integrity, respectively. Hoechst dye (1:20 000) was also added to the printed construct, and together incubated for 15 min at 37 C and humidify atmosphere and immediately imaged.

Visualization of endothelial tight junctions and focal adhesion both in the microfluidic channel and 96-well plates was assessed by immunofluorescence imaging. The device was disconnected from the syringe pump and the microfluidic channels were washed with PBS. Cells inside the channels were fixed in 4% paraformaldehyde (PFA) for 20 min at RT and permeabilized for 10 min in 0.1% Triton X-100. Cells were then blocked for 1 h with BlockAid Blocking Solution (Thermofisher, Cat.No. B10710) and incubated overnight at 4 C with ZO-1 (1:200 in 3% BSA; Abcam, Cat. No. ab221547) or Vinculin (1:400 in 3% BSA, Sigma-Aldrich Cat. No. V9264). Cells were then co-incubated with a secondary-antibodies and Phalloidin-TRITC, (1:10 000; Sigma- Aldrich, Cat. No. P1951) for 1 h in the dark. Nuclei were stained with Hoechst.

Morphological Analysis: Morphological analysis was performed on Human Glioblastoma A-172 and hCMEC/D3 cells to evaluate parameters such as area (A), shape index (SI), and Tortuosity index (TI).[84,85] The cell outline was manually extracted using ImageJ software by selecting the peripheral actin filaments in fluorescence images. Cell area, shape index, and perimeter were then measured automatically. Also, the major and minor axes of the equivalent ellipse for the cell outline were determined.

The SI is defined as follows:

$$SI = \frac{4\pi A}{P^2} \tag{4}$$

where A is the cell area and P the cell perimeter. The SI is equal to 1 for the perfect circle and approaches zero for highly elongated shape.

The TI is defined as follows:

$$TI = \frac{P}{P'} \tag{5}$$

where P is the cell perimeter and P' the equivalent ellipse perimeter of the cell. The equivalent ellipse has equal area and equal moment of inertia to the corresponding extracted cell shape. The TI increases from 1 when the cell shape becomes more tortuous, while the TI is 1 when the cell shape approaches the smooth profile of a circle or an ellipse. Morphological parameters were measured from 50 cells in 8 different fluorescence images for each experimental condition.

Spheroid Formation Analysis: To capture the complex dynamic of GBM invasion into the surrounding brain tumor environment, a quantitative analysis on GBM spheroids formation has been performed using ImageJ software. After bioprinting procedures, the 96-well plates were placed on the RPM device and monitored over time for 72 h using a fluorescence microscope (Nikon Ti inverted fluorescence microscope). Fluorescence images of cells stained with Hoechst were then post processed using ImageJ software and binary images were created for quantification of spheroids dimension around the tumor by counting the white pixels corresponding to a single spheroid in each binarized image.

In-Cell Western Analysis: Quantitative analysis of proteins expression was carried out using the rapid and high-throughput, In-Cell Western (Odyssey) as per manufactures instructions. Briefly, cells were plated at a density of 5×10^3 cells per well and cultured overnight. Plates were then placed on the RPM device and subjected to microgravity. The cells where then fixed with 4% PFA for 20 min and permeabilized with five washed of PBS containing 0.1% Triton X-100 (v/v) for 5 min per wash. Cells were then blocked in Odyssey Blocking Buffer for 90 min at RT and incubated overnight at 4 °C with antibodies against Z0-1 (1:200), active (non-phosphorylated) Yap1 (1:200; Abcam, Cat.No. ab205270), or Vinculin (1:400; Sigma-Aldrich, Cat. No. V9131). Cells were washed with PBS + 0.1% Tween 20 for 5 min and stained with IRDye secondary antibodies (1:200). Finally, the plates were scanned with the Odyssey CLX system (Li-Cor Biosciences) equipped with a near-infrared light technology for signal detection. Signal intensity was quantified with Image Studio software (Version 4.0; Li-Cor), according to the manufacturer's instructions.

Statistical Analysis: The statistical analysis of the data was performed using one-way analysis of variance (ANOVA) with Turkey's test for multiple comparisons, using GraphPad Prism 7.04 for Windows. Average values of at least three independent experiments $\pm$ SEM are shown for each of the assays, that is, vascular permeability assay, Proliferation assay and In-cell Western analysis. Morphological parameters were measured from 50 cells in 8 different fluorescence images for each experimental condition. *P*-value is reported for statistical significance. Comparisons between samples were considered to be statistically significant if the *p*-value was $*p < 0.05$, $**p < 0.01$, $***p < 0.001$.

Supporting Information

Supporting Information is available from the Wiley Online Library or from the author.

Conflict of Interest

The authors declare no conflict of interest.

Data Availability Statement

Research data are not shared.

[1] P. Erkoc, A. Cingöz, T. Bagci-Onder, S. Kizilel, *Macromol. Biosci.* **2017**, *17*, 1600267.

[2] Q. T. Ostrom, H. Gittleman, J. Xu, C. Kromer, Y. Wolinsky, C. Kruchko, J. S. Barnholtz-Sloan, *Neuro-Oncology* **2016**, *18*, v1.

[3] E. Ladomersky, D. M. Scholtens, M. Kocherginsky, E. A. Hibler, E. T. Bartom, S. Otto-Meyer, L. Zhai, K. L. Lauing, J. Choi, J. Sosman, *Front. Pharmacol.* **2019**, *10*, 200.

[4] M. E. Davis, *Clin. J. Oncol. Nurs.* **2016**, *20*, S2.

[5] C. P. Haar, P. Hebbar, G. C. Wallace, A. Das, W. A. Vandergrift, J. A. Smith, P. Giglio, S. J. Patel, S. K. Ray, N. L. Banik, *Neurochem. Res.* **2012**, *37*, 1192.

[6] Y. P. Ramirez, J. L. Weatherbee, R. T. Wheelhouse, A. H. Ross, *Pharmaceuticals* **2013**, *6*, 1475.

[7] I. Paw, R. C. Carpenter, K. Watabe, W. Debinski, H.-W. Lo, *Cancer Lett.* **2015**, *362*, 1.

[8] S. L. Perrin, M. S. Samuel, B. Koszyca, M. P. Brown, L. M. Ebert, M. Oksdath, G. A. Gomez, *Biochem. Soc. Trans.* **2019**, *47*, 625.

[9] W. M. Pardridge, *NeuroRx* **2005**, *2*, 3.

[10] J. Keaney, M. Campbell, *FEBS J.* **2015**, *282*, 4067.

[11] J. D. Huber, R. D. Egleton, T. P. Davis, *Trends Neurosci.* **2001**, *24*, 719.

[12] Y. Hashimoto, K. Tachibana, M. Kondoh, *Drug Discovery Today* **2020**, *25*, 1477.

[13] C. M. Niessen, *J. Invest. Dermatol.* **2007**, *127*, 2525.

[14] P. M. Watson, J. M. Anderson, C. M. Vanltallie, S. R. Doctrow, *Neurosci. Lett.* **1991**, *129*, 6.

[15] O. Tornavaca, M. Chia, N. Dufton, L. O. Almagro, D. E. Conway, A. M. Randi, M. A. Schwartz, K. Matter, M. S. Balda, *J. Cell Biol.* **2015**, *208*, 821.

[16] D. Vestweber, *Arterioscler., Thromb., Vasc. Biol.* **2008**, *28*, 223.

[17] E. Tzima, M. Irani-Tehrani, W. B. Kiosses, E. Dejana, D. A. Schultz, B. Engelhardt, G. Cao, H. DeLisser, M. A. Schwartz, *Nature* **2005**, *437*, 426.

[18] L. Cucullo, M. Hossain, V. Puvenna, N. Marchi, D. Janigro, *BMC Neurosci.* **2011**, *12*, 40.

[19] J. G. DeStefano, Z. S. Xu, A. J. Williams, N. Yimam, P. C. J. F. Searson, *Fluids Barriers CNS* **2017**, *14*, 20.

[20] S. Santaguida, D. Janigro, M. Hossain, E. Oby, E. Rapp, L. Cucullo, *Brain Res.* **2006**, *1109*, 1.

[21] A. Parodi, M. Rudzińska, A. A. Deviatkin, S. M. Soond, A. V. Baldin, A. A. Zamyatnin, *Pharmaceutics* **2019**, *11*, 245.

[22] N. Abbott, *J. Inherited Metab. Dis.* **2013**, *36*, 437.

[23] O. Van Tellingen, B. Yetkin-Arik, M. De Gooijer, P. Wesseling, T. Wurdinger, H. De Vries, *Drug Resist. Updates* **2015**, *19*, 1.

[24] H. Huang, R. D. Kamm, R. T. Lee, *Am. J. Physiol.: Cell Physiol.* **2004**, *287*, C1.

[25] A.-L. Le Roux, X. Quiroga, N. Walani, M. Arroyo, P. Roca-Cusachs, *Philos. Trans. R. Soc., B* **2019**, *374*, 20180221.

[26] E. Afshinnekoo, R. T. Scott, M. J. MacKay, E. Pariset, E. Cekanaviciute, R. Barker, S. Gilroy, D. Hassane, S. M. Smith, S. R. Zwart, *Cell* **2020**, *183*, 1162.

[27] P. Bradbury, H. Wu, J. U. Choi, A. E. Rowan, H. Zhang, K. Poole, J. Lauko, J. Chou, *Front. Cell Dev. Biol.* 2020, *8*, 96.

[28] D. Grimm, J. Bauer, P. Kossmehl, M. Shakibaei, J. Schönberger, H. Pickenhahn, G. Schulze-Tanzil, R. Vetter, C. Eilles, M. Paul, *FASEB J.* **2002**, *16*, 604.

[29] J. Vassy, S. Portet, M. Beil, G. Millot, F. Fauvel-Lafeve, G. Gasset, D. Schoevaert, *Adv. Space Res.* **2003**, *32*, 1595.

[30] P. A. Plett, R. Abonour, S. M. Frankovitz, C. M. Orschell, *Exp. Hematol.* **2004**, *32*, 773.

[31] M. Infanger, P. Kossmehl, M. Shakibaei, S. Baatout, A. Witzing, J. Grosse, J. Bauer, A. Cogoli, S. Faramarzi, H. Derradji, *Apoptosis* **2006**, *11*, 749.

[32] Z.-x. Shi, W. Rao, H. Wang, N.-d. Wang, J.-W. Si, J. Zhao, J.-c. Li, Z.-r. Wang, *Biochem. Biophys. Res. Commun.* **2015**, *457*, 378.

[33] X. Tan, A. Xu, T. Zhao, Q. Zhao, J. Zhang, C. Fan, Y. Deng, A. Freywald, H. Genth, J. Xiang, *Sci. Rep.* **2018**, *8*, 3769.

[34] K. Konstantopoulos, S. N. Thomas, *Annu. Rev. Biomed. Eng.* **2009**, *11*, 177.

[35] P. Lu, V. M. Weaver, Z. Werb, *J. Cell Biol.* **2012**, *196*, 395.

[36] J. M. Northcott, I. S. Dean, J. K. Mouw, V. M. Weaver, *Front. Cell Dev. Biol.* **2018**, *6*, 17.

[37] G. Apodaca, *Am. J. Physiol.: Renal, Fluid Physiol.* **2002**, *282*, F179.

[38] S. Chien, *Am. J. Physiol.: Heart Circ. Physiol.* **2007**, *292*, H1209.

[39] S. Mo, C.-C. Coussios, L. Seymour, R. J. Carlisle, *Expert Opin. Drug Delivery* **2012**, *9*, 1525.

[40] Y. Zhang, J. Yu, H. N. Bomba, Y. Zhu, Z. Gu, *Chem. Rev.* **2016**, *116*, 12536.

[41] G. Silvani, C. Scognamiglio, D. Caprini, L. Marino, M. Chinappi, G. Sinibaldi, G. Peruzzi, M. F. Kiani, C. M. Casciola, *Small* **2019**, *15*, 1905375.

[42] K. Duval, H. Grover, L.-H. Han, Y. Mou, A. F. Pegoraro, J. Fredberg, Z. Chen, *Physiology* **2017**, *32*, 266.

[43] M. E. Katt, A. L. Placone, A. D. Wong, Z. S. Xu, P. C. Searson, *Front. Bioeng. Biotechnol.* **2016**, *4*, 12.

[44] D. Truong, *Biomaterials* **2019**, *198*, 63.

[45] D. Huh, B. D. Matthews, A. Mammoto, M. Montoya-Zavala, H. Y. Hsin, D. E. Ingber, *Science* **2010**, *328*, 1662.

[46] S. N. Bhatia, D. E. Ingber, *Nat. Biotechnol.* **2014**, *32*, 760.

[47] N. S. Bhise, J. Ribas, V. Manoharan, Y. S. Zhang, A. Polini, S. Massa, M. R. Dokmeci, A. Khademhosseini, *J. Controlled Release* **2014**, *190*, 82.

[48] K. Yum, S. G. Hong, K. E. Healy, L. P. Lee, *Biotechnol. J.* **2014**, *9*, 16.

[49] Y. Kang, P. Datta, S. Shanmughapriya, I. T. Ozbolat, *ACS Appl. Bio Mater.* **2020**, *3*, 5552.

[50] S. Knowlton, A. Joshi, B. Yenilmez, I. T. Ozbolat, C. K. Chua, A. Khademhosseini, S. Tasoglu, *Int. J. Bioprint.* **2016**, *2*, 3.

[51] S. Mao, Y. Pang, T. Liu, Y. Shao, J. He, H. Yang, Y. Mao, W. B. Sun, *Biofabrication* **2020**, *12*, 042001.

[52] Y. C. Oztan, N. Nawafleh, Y. Zhou, P. Y. Liyanage, S. D. Hettiarachchi, E. S. Seven, R. M. Leblanc, A. Ouhtit, E. Celik, *Bioprinting* **2020**, *18*, e00079.

[53] J. Li, C. Parra-Cantu, Z. Wang, Y. S. Zhang, *Trends Cancer* **2020**, *6*, 745.

[54] C. Lee, E. Abelseth, L. De La Vega, S. Willerth, *Mater. Today Chem.* **2019**, *12*, 78.

[55] H.-G. Yi, Y. H. Jeong, Y. Kim, Y.-J. Choi, H. E. Moon, S. H. Park, K. S. Kang, M. Bae, J. Jang, H. Youn, *Nat. Biomed. Eng.* **2019**, *3*, 509.

[56] D. Hambardzumyan, G. Bergers, *Trends Cancer* **2015**, *1*, 252.

[57] A. Abu Taha, H.-J. Schnittler, *Cell Adhes. Migr.* **2014**, *8*, 125.

[58] J. S. Jeon, S. Bersini, M. Gilardi, G. Dubini, J. L. Charest, M. Moretti, R. D. Kamm, *Proc. Natl. Acad. Sci. USA* **2015**, *112*, 214.

[59] H. Lee, W. Park, H. Ryu, N. L. Jeon, *Biomicrofluidics* **2014**, *8*, 054102.

[60] H. Schnittler, M. Taha, M. O. Schnittler, A. A. Taha, N. Lindemann, J. Seebach, *Cell Tissue Res.* **2014**, *355*, 529.

[61] G. Silvani, V. Romanov, C. D. Cox, B. Martinac, *Front. Bioeng. Biotechnol.* **2020**, *9*, 21.

[62] P. J. Gaillard, A. G. de Boer, *Eur. J. Pharm. Sci.* **2000**, *12*, 95.

[63] C. Lohmann, S. Hüwel, H.-J. Galla, *J. Drug Targeting* **2002**, *10*, 263.

[64] X. Wang, B. Xu, M. Xiang, X. Yang, Y. Liu, X. Liu, Y. Shen, *Microvasc. Res.* **2020**, *128*, 103930.

[65] L. Shi, M. Zeng, Y. Sun, B. M. Fu, *J. Biomech. Eng.* **2014**, *136*, 031005.

[66] A. Thomas, S. Wang, S. Sohrabi, C. Orr, R. He, W. Shi, Y. Liu, *Biomicrofluidics* **2017**, *11*, 024102.

[67] A. Carisey, C. Ballestrem, *Eur. J. Cell Biol.* **2011**, *90*, 157.

[68] R. Abylkassov, Y. Xie, *Oncol. Lett.* **2016**, *12*, 2277.

[69] Y. Lv, K. Kim, Y. Sheng, J. Cho, Z. Qian, Y.-Y. Zhao, G. Hu, D. Pan, A. B. Malik, G. Hu, *Circ. Res.* **2018**, *123*, 43.

[70] T. Azad, M. Ghahremani, X. Yang, *Cells* **2019**, *8*, 407.

[71] C. D. Arvanitis, G. B. Ferraro, R. K. Jain, *Nat. Rev. Cancer* **2020**, *20*, 26.

[72] L. P. Ganipineni, F. Danhier, V. J. Préat, *J. Controlled Release* **2018**, *281*, 42.

[73] G. F. Woodworth, G. P. Dunn, E. A. Nance, J. Hanes, H. Brem, *Front. Oncol.* **2014**, *4*, 126.

[74] X. Cai, R. G. Briggs, H. B. Homburg, I. M. Young, E. J. Davis, Y.-H. Lin, J. D. Battiste, M. E. Sughrue, *Biomed. Microdevices* **2020**, *22*, 60.

[75] M. Oksdath, S. L. Perrin, C. Bardy, E. F. Hilder, C. A. DeForest, R. D. Arrua, G. A. Gomez, *APL Bioeng.* **2018**, *2*, 041501.

[76] Y. Wang, L. Wang, Y. Guo, Y. Zhu, J. Qin, *RSC Adv.* **2018**, *8*, 1677.

[77] S. Han, S. Kim, Z. Chen, H. K. Shin, S.-Y. Lee, H. E. Moon, S. H. Paek, S. Park, *Int. J. Mol. Sci.* **2020**, *21*, 2993.

[78] O. Tricinci, D. De Pasquale, A. Marino, M. Battaglini, C. Pucci, G. Ciofani, *Adv. Mater. Technol.* **2020**, *5*, 2000540.

[79] M. Z. Nassef, S. Kopp, M. Wehland, D. Melnik, J. Sahana, M. Krüger, T. J. Corydon, H. Oltmann, B. Schmitz, A. Schütte, *Int. J. Mol. Sci.* **2019**, *20*, 3156.

[80] P. M. Gershovich, J. G. Gershovic, L. B. Buravkova, *Life Space Life Earth* **2008**, *553*, 68.

[81] S. Dupont, L. Morsut, M. Aragona, E. Enzo, S. Giulitti, M. Cordenonsi, F. Zanconato, J. Le Digabel, M. Forcato, S. J. N. Bicciato, *Nature* **2011**, *474*, 179.

[82] F. Zanconato, M. Cordenonsi, S. Piccolo, *Cancer Cell* **2016**, *29*, 783.

[83] T. G. Walsh, R. P. Murphy, P. Fitzpatrick, K. D. Rochfort, A. F. Guinan, A. Murphy, P. M. Cummins, *J. Cell. Physiol.* **2011**, *226*, 3053.

[84] J. F. Cornhill, M. J. Levesque, E. E. Herderick, R. M. Nerem, J. W. Kilman, J. Vasko, *Atherosclerosis* **1980**, *35*, 321.

[85] Y. Sugaya, N. Sakamoto, T. Ohashi, M. Sato, *JSME Int. J., Ser. C* **2003**, *46*, 1248.